



# High uniformity magnetic coil for search of neutron electric dipole moment

A. Pérez Galván<sup>a,\*</sup>, B. Plaster<sup>b</sup>, J. Boissevain<sup>a</sup>, R. Carr<sup>a</sup>, B.W. Filippone<sup>a</sup>, M.P. Mendenhall<sup>a</sup>,  
R. Schmid<sup>a</sup>, R. Alarcon<sup>c</sup>, S. Balascuta<sup>c</sup>

<sup>a</sup> W.K. Kellogg Radiation Laboratory, California Institute of Technology, Pasadena, CA, 91125, USA

<sup>b</sup> Department of Physics and Astronomy, University of Kentucky, Lexington, KY, 40506, USA

<sup>c</sup> Department of Physics, Arizona State University, Tempe, AZ 85287, USA

## ARTICLE INFO

### Article history:

Received 12 July 2011

Received in revised form

1 September 2011

Accepted 12 September 2011

Available online 21 September 2011

### Keywords:

Electric dipole moment

Magnetic fields

Magnetic gradients

High uniformity

## ABSTRACT

We present in this article a prototype magnetic coil that has been developed for a new search for the electric dipole moment of the neutron at the Spallation Neutron Source at Oak Ridge National Laboratory. The gradients of the magnetic field generated by the coil have been optimized to reduce known systematic effects and to yield long polarization lifetimes of the trapped particles sampling the highly uniform magnetic field. Measurements of the field uniformity of this prototype magnetic coil are also presented.

© 2011 Elsevier B.V. All rights reserved.

## 1. Introduction

A discovery of a neutron electric dipole moment (nEDM) in the next generation of experiments [1] would represent a new source of charge conjugation and parity (CP) violation, and potentially, new physics beyond the Standard Model of elementary particles [2,3]. In addition, the existence of a nEDM might also explain the mystery behind the matter-antimatter asymmetry of the Universe [4].

Given the important implications of an observation of a non-zero nEDM a new experimental effort is underway [5]. It will take place at the Spallation Neutron Source (SNS) at Oak Ridge National Laboratory. Like most nEDM experiments, it will search for a change in the Larmor frequency of trapped Ultra-Cold Neutrons (UCNs) correlated with the orientation of an electric field with respect to a magnetic field. However, this measurement is based on several new techniques [6] that promise to increase the sensitivity by two orders of magnitude below the current best limit ( $2.9 \times 10^{-26}$  e cm at a 90% confidence level [7]).

We summarize in this article the requirements and design optimization that will be used to develop the coil that will provide the main holding field for the experiment. The design optimization described here takes into account systematic effects related to imperfections of the magnetic field environment. Furthermore, we present results from performance tests of a prototype half scale version of the coil.

## 2. Magnetic coil requirements

### 2.1. Overview of the experiment

Experimental searches for a permanent electric dipole moment using trapped UCNs (neutrons with a kinetic energy below 200 neV) [8] can give orders of magnitude more sensitivity due to a longer interaction time (hundreds of seconds instead of a few milliseconds as in neutron beam experiments). Experiments using trapped UCNs also suppress systematic effects due to the motional magnetic field [9–11] and misalignment of electric and magnetic fields [12].

The new experiment to be carried out at the SNS uses polarized UCNs in a bath of superfluid  $^4\text{He}$  at a temperature of around 450 mK contained in two identical storage cells. The rectangular cells are immersed in a highly uniform magnetic field with a magnitude of 1–5  $\mu\text{T}$  generated by a cylindrical coil. A set of electrodes provides the electric field. The electrode configuration is such that each cell sees the same electric field in magnitude but with opposite sign. The rectangular dimensions of each cell are  $L_x=7.5$  cm,  $L_y=12.5$  cm, and  $L_z=40$  cm. The longest dimension of the cells is oriented along the axis of the magnetic coil and the shortest along the quantization axis set by the magnetic field (see Fig. 1). An admixture of highly dilute polarized  $^3\text{He}$  atoms is stored in the same volume serving as an analyzer [13,14] and as a comagnetometer [15].

All of the particles start with their spins aligned with the holding field. A  $\pi/2$  pulse rotates both species onto a plane perpendicular to the holding field. The UCNs and  $^3\text{He}$  particles

\* Corresponding author. Tel.: +1 6263954276; fax: +1 626 5648708.  
E-mail address: [apg@caltech.edu](mailto:apg@caltech.edu) (A. Pérez Galván).

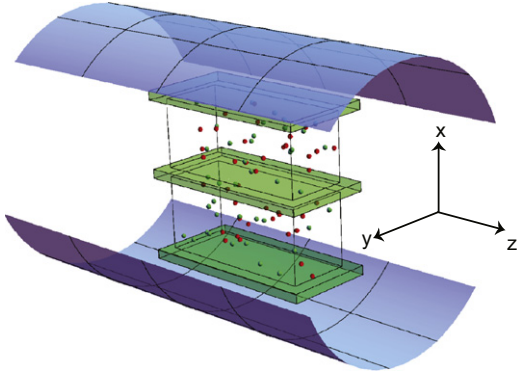


**Fig. 1.** Schematic setup of the experiment. The three plates represent the electrodes. The middle plate is set at a non-zero voltage and the outer plates are set to ground. The region between the plates represents the measurement cells with UCNs and  $^3\text{He}$  atoms (depicted with different colors). The enclosing cylinder is the magnetic coil which is shown schematically. (For interpretation of the references to color in this figure legend, the reader is referred to the web version of this article.)

then precess with frequencies given by

$$\omega_n = -2(\mu_n B \pm d_n E)/\hbar, \quad (1)$$

$$\omega_{\text{He}} = -2\mu_{\text{He}} B/\hbar, \quad (2)$$

where  $\omega_n(\omega_{\text{He}})$  is the Larmor frequency of the neutron ( $^3\text{He}$  atom),  $\mu_n(\mu_{\text{He}})$  is the magnetic dipole moment of the neutron [ $^3\text{He}$  atom [17]],  $d_n$  is the electric dipole moment of the neutron (the electric dipole moment of the  $^3\text{He}$  atom is much smaller than the neutron and assumed zero for this discussion [18]),  $B$  is the magnetic field, and  $E$  is the electric field. Eqs. (1) and (2) show that a precise and accurate measurement depends on the control and quality of the magnetic field environment observed by the particles [19].

The detection technique measures the difference in the Larmor frequencies of both species by monitoring the ultraviolet scintillation produced by the  $n + ^3\text{He} \rightarrow p + t$  reaction in superfluid  $^4\text{He}$  [13,14]. The capture rate is a function of the angle between the spins of the particles with the capture probability maximized when both spins are antialigned. Hence, the scintillation will be amplitude-modulated with a frequency given by  $\Delta\omega = \omega_{\text{He}} - \omega_n$ . A non-zero nEDM will “pull” the frequency  $\Delta\omega$  in correlation with the orientation of the electric field with respect to the magnetic field. In other words, one cell will observe an increase in the frequency while the other will observe a decrease.

## 2.2. Holding field requirements

Although analytical expressions for current distributions that yield uniform magnetic fields exist (infinite solenoid, cosine distribution of current on the surface of an infinite cylinder), the experimenter has to accept that any type of winding will have a finite size and imperfections that will give a non-uniform magnetic field. These are characterized by the size of the gradients inside the volume where the measurement will take place and they can be tailored to satisfy the requirements of the experiment at hand [20]. For the nEDM experiment, the specifications of the magnetic field gradients are determined by two requirements: long polarization lifetimes of the particles inside the experimental volumes and the size of the known systematic effects related to magnetic field gradients.

### 2.2.1. Relaxation of polarization

The relaxation rate of the polarization of a sample of confined particles in a magnetic field is influenced by the gradients of the field [21–23]. A much smaller effect has also been predicted for

perfectly uniform magnetic and electric fields that should be taken into account for very long relaxation times [24]. Moving particles observe a magnetic field gradient as a time-dependent magnetic field which induces a rotation of the spin direction and thus decreases the overall polarization. McGregor [22] has developed a formalism to estimate the longitudinal  $T_1$  and transverse  $T_2$  polarization lifetimes of particles in non-homogeneous magnetic fields under different geometries. Since  $T_1$  is longer than  $T_2$ , the latter sets the primary constraints on the magnetic field gradients. If the direction of the holding field is in the  $x$  direction, then  $T_2$  is given by [22]

$$\frac{1}{T_2} = \frac{1}{2T_1} + \frac{\gamma_i^2}{2} \left( S_x(0) \left\langle \left| \frac{\partial B_x}{\partial x} \right|^2 \right\rangle_{\text{vol}} + S_y(0) \left\langle \left| \frac{\partial B_x}{\partial y} \right|^2 \right\rangle_{\text{vol}} + S_z(0) \left\langle \left| \frac{\partial B_x}{\partial z} \right|^2 \right\rangle_{\text{vol}} \right),$$

where  $\langle \dots \rangle_{\text{vol}}$  represents a volume average,  $\gamma_i$  is the gyromagnetic ratio of the particles ( $^3\text{He}$  or UCNs) and  $S_j(0)$  is the positional autocorrelation function at zero frequency in the  $j$ th direction.

The positional autocorrelation function depends on how fast the particle samples the magnetic environment. The faster it samples the volume, the less correlated the rotations induced by the gradients are. Under our experimental conditions, the  $^3\text{He}$  atoms diffuse very slowly colliding with phonons from the  $^4\text{He}$  bath. The  $^3\text{He}$  atoms completely diffuse ( $\tau_{\text{He}}^{\text{He}} \approx L_z^2/D(T)$  where  $D$  is the temperature dependent diffusion constant [25]) over the experimental volume in seconds. In contrast, UCNs do so in tens of milliseconds. Hence, we expect the  $^3\text{He}$  depolarization to be dominant over the UCN relaxation.

Following McGregor [22], the polarization relaxation rate for  $^3\text{He}$  atoms is given by

$$\frac{1}{T_2} \approx \frac{\gamma_{\text{He}}^2 L_z^4}{120D} \left\langle \left| \frac{\partial B_x}{\partial z} \right|^2 \right\rangle_{\text{vol}}, \quad (3)$$

where we have assumed that  $1/2T_1$  is negligible and that the dominant component in the sum is set by the longer dimension of the cells. Evaluating Eq. (3) with  $D = 1.6/T^7 \text{ cm}^2/\text{s}$  [25] at 0.45 K and  $L_z = 40 \text{ cm}$  gives a gradient of the order of 10 pT/cm for a lifetime of the order of  $10^4 \text{ s}$ .

### 2.2.2. Frequency shifts induced by magnetic field gradients

One of the most serious systematic effects is the coupling between magnetic field gradients and the motional magnetic field  $\vec{B}_m = \vec{v} \times \vec{E}/c^2$  [9–11]. This effect shifts the Larmor frequency in correlation with the size and direction of the electrical field, just like an electric dipole moment would. The details of the calculation depend on the geometry of the cells, the trajectories of the particles, and their velocity distribution. However, it is possible to estimate the size of the effect for cylindrical geometries for UCNs with the formula [9–11]

$$d_f \sim -\frac{\nu^2 \hbar}{8c^2 B_0^2} \left\langle \frac{\partial B_x}{\partial x} \right\rangle_{\text{vol}}, \quad (4)$$

where  $d_f$  is the false electric dipole moment,  $\nu$  is the average velocity of the UCNs,  $c$  is the speed of light, and  $x$  is the direction of the holding field  $B_0$ . This sets a limit on the size of the allowed gradient  $\langle \partial B_x / \partial x \rangle_{\text{vol}}$  to less than 10 pT/cm in a magnetic field of 3  $\mu\text{T}$  for a  $d_f \approx 3 \times 10^{-28} \text{ e cm}$ . This represents a fractional gradient of 3.3 ppm/cm (see Subsection 4.2).

## 3. Design optimization and construction

### 3.1. Finite element analysis studies

We base our design on a cylindrical “cos( $\theta$ )” coil where the angular distribution of the wires follows a discrete cosine distribution. This configuration offers a highly uniform field transverse to the

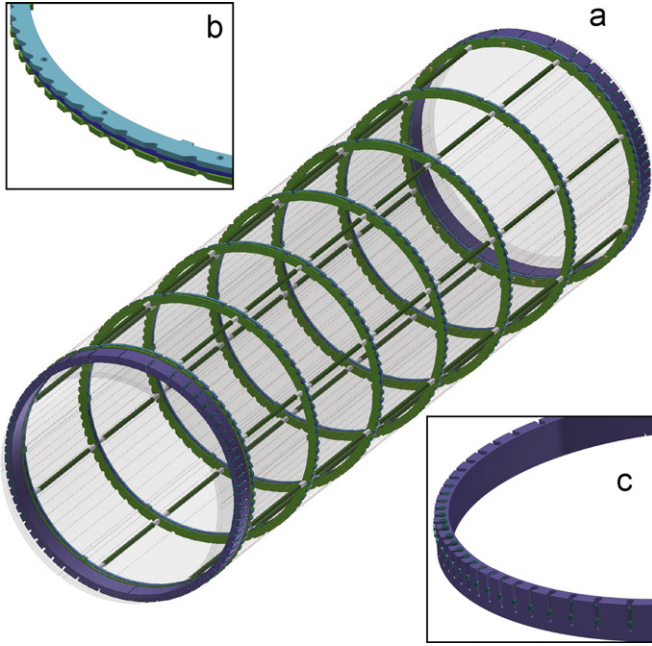


**Fig. 2.** (a) Schematic view of the  $\cos(\theta)$  coil. (b) Detail of the positioner ring. (c) Detail of the tensioner ring.

axis of the coil and has greater access for all the services for the experiment. The wires run axially on the surface of a cylinder and bend along the circumference of the end caps (rather than across) leaving open access to the interior (see Fig. 2). The coil is concentric with a superconducting and a ferromagnetic shield. Analysis shows that image currents generated at the superconductor deteriorate the uniformity of the field. A ferromagnetic shield between the superconducting shield and the coil help restore the uniformity.

The optimization consists of minimizing the volume gradients as a function of angular distribution of the wires, length to radius ratio ( $L/R$ ), and number of wires of the coil. We design our configuration using a commercially available finite element analysis package (TOSCA) and a code developed by our group [26]. We find that the angular distribution of the wires needs to depart from a standard cosine distribution to match the imposed boundary conditions (set by the ferromagnetic and superconducting shields) and the requirements on the gradients. A single parameter  $K \ll 1$  quantifies the deviation from a standard  $\cos(\theta)$  distribution. [26] The analysis with both approaches gives consistent results and determines that 60 wires (or 30 “turns”) (see Table 1) and a modified cosine distribution with  $L/R=6.49$  are sufficient to satisfy the stringent requirements.

Simulations on the accuracy of the position of the wires determine that it is necessary to add “trimming” coils to compensate for residual non-uniformities due to imperfections in the winding. The trimming coils consist of  $\cos(\theta)$  coils with fewer wires that match the angular position of the larger coil. This is only possible in certain cases where the total number of wires  $N$  in a quadrant of the circumference is equal to  $n_1 \cdot n_2$  where  $n_1$  is an odd number. The number of wires in a quadrant of the matching coil will be given by  $n_2$  (see Appendix A). For 15 wires per quadrant, 3 sets of trimming coils can be added with 1 (corresponding to  $15 \times 1$ ), 3, and 5 ( $5 \times 3$ ) wires per quadrant. Table 2 shows the angular positions of the trimming coils in terms of the angles of the main coil.

### 3.2. Construction

We constructed a prototype half scale version of the coil with the results from numerical simulation. Five positioner rings, two

**Table 1**

Angular distribution of wires for the modified  $\cos(\theta)$  coil. Only the angles for two quadrants are shown, the rest can be obtained by adding  $180^\circ$  to the values. For example,  $\theta_{31} = \theta_1 + 180$ .

Angle (deg)		Angle (deg)	
$\theta_1$	14.9779	$\theta_{16}$	91.8912
$\theta_2$	26.0680	$\theta_{17}$	95.6823
$\theta_3$	33.8224	$\theta_{18}$	99.5001
$\theta_4$	40.2275	$\theta_{19}$	103.3637
$\theta_5$	45.8601	$\theta_{20}$	107.2939
$\theta_6$	50.9848	$\theta_{21}$	111.3150
$\theta_7$	55.7496	$\theta_{22}$	115.4557
$\theta_8$	60.2481	$\theta_{23}$	119.7519
$\theta_9$	64.5443	$\theta_{24}$	124.2504
$\theta_{10}$	68.6850	$\theta_{25}$	129.0152
$\theta_{11}$	72.7061	$\theta_{26}$	134.1399
$\theta_{12}$	76.6363	$\theta_{27}$	139.7725
$\theta_{13}$	80.4999	$\theta_{28}$	146.1776
$\theta_{14}$	84.3177	$\theta_{29}$	153.9320
$\theta_{15}$	88.1088	$\theta_{30}$	165.0221

**Table 2**

Angular distribution of wires for the modified  $\cos(\theta)$  trimming coils. The angles refer to the main coil. Only the angles for two quadrants are shown, the rest can be obtained by adding  $180^\circ$  to the values. For example,  $\theta_{32} = \theta_2 + 180$ .

Wires per quadrant	Angle
1	$\theta_8, \theta_{23}$
3	$\theta_3, \theta_8, \theta_{13}, \theta_{18}, \theta_{23}, \theta_{28}$
5	$\theta_2, \theta_5, \theta_8, \theta_{11}, \theta_{14}, \theta_{17}, \theta_{20}, \theta_{23}, \theta_{26}, \theta_{29}$

tensioner rings, several spacer rods, and 150 m of 28 AWG copper wire with insulation on a machined acrylic cylinder form a  $\cos(\theta)$  coil (from here on referred to as the  $B_0$  coil). This unusual configuration follows from the requirement of cryogenic operation of the magnet coil, i.e. it is necessary to compensate for deformation under thermal contraction when cooling from room temperature to 4 K.

The wire that carries the current is held in place by five positioner rings and two tensioner rings (see Fig. 2). All of these items slide into position following four keyways machined on a 2.26 m long acrylic cylinder with a radius of 30.5 cm and are axially separated by spacer rods at roughly 35.3 cm intervals. The positioner rings themselves are composed of three parts that locate the wire (see inset of Fig. 2) and have been machined to match the angular distribution determined through numerical analysis. At both ends of the acrylic cylinder tensioner rings with spring loaded pins keep the wire under tension.

The spacer rods between the positioner rings are made of two different materials (nylon and G10) to match the thermal contraction of the copper wire that carries the current. The rings and pins are made out of acrylic to reduce weight and to match the thermal contraction of the cylindrical form. The complete ensemble is free to slide on the acrylic cylinder following the thermal contraction of the wire. Fig. 3 shows the completed prototype half scale coil. We also wind two sets of trimming coils to compensate for imperfections (1 and 3 wires per quadrant). Both sets share the “grooves” of the  $B_0$  coil so no extra machining is necessary.

The ferromagnetic shield encloses the  $B_0$  coil and improves the uniformity of the magnetic field. It is made out of 3 layers of overlapping metglas 2750 M [27] ribbons 5.1 cm wide and 22  $\mu\text{m}$  thick with a magnetic saturation value of 0.77 T. The metglas ribbons are attached with Kapton tape to a PVC-like [28] cylinder with a diameter of 66 cm. The length of the shield is 2.20 m.



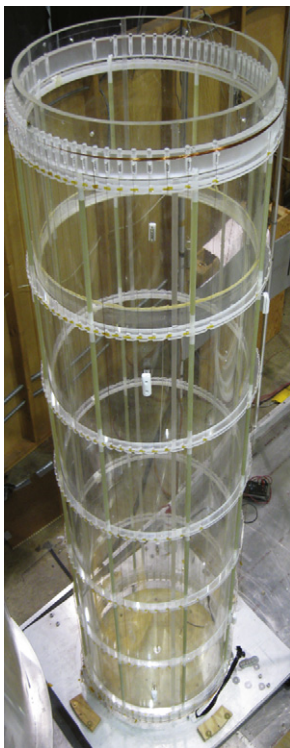


Fig. 3. Photograph of the half scale version of the  $B_0$  coil.

The first two metglas layers are wound in the azimuthal direction and the final one in the axial direction to improve axial shielding [29]. This geometrical configuration allows us to avoid saturating the metglas for magnetic fields less or equal to  $90 \mu\text{T}$  [30]. In addition, comparison between simulated and experimental magnetic field profiles are in good agreement which suggests that the shield is performing in a non-saturating regime. A pair of coils placed at both ends of the ferromagnetic shield (z-coils) help to optimize the  $B_z$  component of the field.

Magnetic contaminants in the cylindrical forms might destroy the magnetic field uniformity. In principle, the trimming coils can compensate for undesired gradients in the fiducial volume independent of their source. Nevertheless, we take precautions to minimize possible issues. The cylinders that support the coil and the ferromagnetic shield are not machined from larger pieces so the probability of finding magnetic contaminants, like pieces of steel embedded in the material, is low. In addition, the larger acrylic rings are cut using a water-jet cutter machine to minimize possible magnetic interference.

Even with these precautions, there remains the problem of gradients generated by unexpected contaminants. They can be classified in two categories: particles with permanent magnetization and particles with induced magnetization. The particles with permanent magnetization should be randomly aligned with respect to the magnetic field generated by the  $B_0$  coil and the gradients generated by them should average out to first order over the fiducial volume. The particles with induced magnetization will contribute a coherent gradient that is proportional to the size of the magnetic field they are experiencing up to a saturating value and that decreases as the fourth power of the distance from the particle. These particles might spoil the uniformity of the magnetic field. To the best of our knowledge, room temperature measurements of the uniformity at high values of the magnetic field ( $10 \mu\text{T} \leq |B_0| \leq 90 \mu\text{T}$ ) inside the cylinders do not show evidence of these type of contaminants. Their influence at lower magnetic fields should be even less relevant.

## 4. Performance tests and results

### 4.1. Experimental procedure

The uniformity required of the  $B_0$  coil makes it difficult to evaluate its performance in a standard laboratory environment. We constructed two large lidless cylindrical magnetic shields, in addition to the ferromagnetic shield, to attenuate the external magnetic field. The diameters of the shields are  $D_1=1.07 \text{ m}$  and  $D_2=1.12 \text{ m}$ . Both have a height of  $2.21 \text{ m}$ . The smaller shield is made out of overlapping metglas ribbons  $5.1 \text{ cm}$  wide and  $22 \mu\text{m}$  thick attached to a cardboard tube. Three layers are wound in the azimuthal direction while one layer is positioned along the length of the cylinder. The larger shield is made out of sheets ( $76.4 \times 101.6 \text{ cm}^2$ ) of annealed mu-metal with a thickness of  $356 \mu\text{m}$ . Sheets of solid foam with a thickness of  $2.54 \text{ cm}$  attached to the cardboard tube on top of the metglas provide a larger cylindrical form to attach the mu-metal. The set of three shields attenuate the external field by a factor of 650 for the transverse direction and 30 for the axial direction.

We measure the components of the magnetic field inside the fiducial volume with a 3-axis fluxgate magnetometer from Bartington [31]. The magnetometer measures the three components of the magnetic field simultaneously using three orthogonal fluxgate magnetometers. The orthogonality error between each fluxgate is less than  $0.1^\circ$ . In our coordinate system, the field generated by the  $B_0$  coil points in the x-direction. The magnetometer is read out with a Signal Conditioning Unit, also from Bartington, that converts the signal of the fluxgate to three voltages (one for each axis) that are simply related by a conversion factor to the magnetic field measured.

We constructed an automated station to evaluate the magnetic field gradients inside the fiducial volume. The station is approximately  $4.5 \text{ m}$  high with a rectangular base (see Fig. 4). The length of the base is  $1.22 \text{ m}$  and it is wide enough to accommodate the complete setup (magnetic shields and coil). The station is made out of aluminum held together with mostly brass screws and pins to reduce the amount of magnetic material at close proximity to the shields. On top of the station we place a computer controlled 3-axis stepper motor from National Instruments with a resolution of  $150 \mu\text{m}$  that moves a  $3 \text{ m}$  long and  $2.54 \text{ cm}$  thick G10 rod to

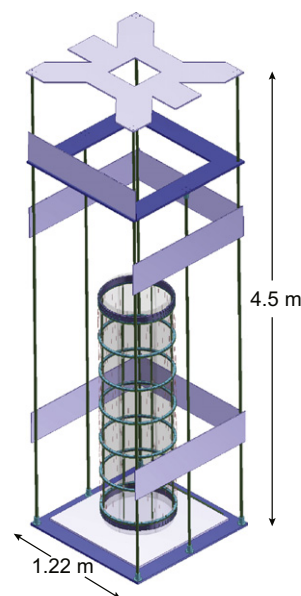


Fig. 4. Automated measurement station with coil (magnetic shields and 3-axis stepper motor not shown).

which we attach the 3-axis magnetometer. The motor is approximately 3 m away from the fiducial volume to minimize magnetic interference. We read out the magnetic field components with three multimeters with a 6.5-digit resolution connected to a computer. With this setup we can measure the magnetic field for long periods of time and high positional precision.

Two low noise current supplies in series from Agilent (model number E3645A) provide the current for the  $B_0$  coil. We monitor the current with a 6.5-digit multimeter to check for fluctuations. We have measured the stability of the current supplies to be better than 100 ppm. The coil generates a magnetic field of approximately 0.54 G/A. Four extra power supplies provide the current for the trimming coils. Typical values of the currents on the trimming coils are of the order of tens of mA. Although in principle we can control each wire of the  $\cos(\theta)$  trimming coils independently to have a higher control of the profile of the magnetic field, we find that we can achieve the desired uniformity with fewer degrees of freedom.

#### 4.2. Results

We optimize the magnetic field profile prior to a full mapping measurement cycle by adjusting the currents of the trimming coils and measuring the uniformity of the  $B_x$  component in the  $x$  direction (holding field direction) and the uniformity of the  $B_z$  component along the  $z$ -axis. The modified  $\cos(\theta)$  trimming coils will affect the  $B_x$  component along the  $x$ -axis while the  $z$ -coil will affect the  $B_z$  component along the  $z$ -axis. Reducing the size of  $\partial B_x/\partial x$  and  $\partial B_z/\partial z$  in a volume also minimizes the  $\partial B_y/\partial y$  component through the relation  $\nabla \cdot \vec{B} = 0$ . The optimization procedure follows from the geometry of the field (due to the tailored  $B_0$  coil). This feature makes the  $B_0$  coil amenable to an *in situ* gradient monitoring system [32].

After each optimization cycle we demagnetize the shields by driving them to saturation using an AC current supply from California Instruments (model number 801RF). The waveform that drives the current is the product of a sine wave and a ramp. Well known procedures like “mechanically shaking” the shields after demagnetization do not improve the magnetic attenuation that we observe nor the noise level probably due to the fact that our outermost layer is not composed of a monolithic mu-metal piece. Fig. 5 shows a sample profile of  $B_x$  before and after trimming. Once the procedure reaches an optimum, we proceed to take data.

A full mapping measurement cycle consists of recording the value of the magnetic field components at several positions inside and close to the boundary of the half scale measurement cells ( $L_x=3.75$  cm,  $L_y=6.2$  cm, and  $L_z=20$  cm). We store the value of each magnetic field component as well as the value of the current of the  $B_0$  coil at the instant a measurement is taken for off-line analysis. We evaluate the magnetic field using two different number of points per cell: 54 and 150 points forming a Cartesian lattice. For 54 points per cell we take (6, 3, 3) points in the ( $x, y, z$ ) directions every (1, 3.5, 10) cm. For 150 points per cell we take (6, 5, 5) points in the ( $x, y, z$ ) directions every (1, 1.8, 5) cm. A higher number of points gives more information of the profile of the magnetic field but takes much longer to do a complete evaluation of both cells (1.5 v. 4 hours). Under equal conditions *i.e.* a quiet, stable environment, both methods yield results that agree within the error bars.

We observe during the experimental runs changes in the magnetic field correlated with noise in the current supplies providing the current for the  $B_0$  coil. We use the stored value of the current to correct for it. We subtract a small magnetic field proportional to the change in current  $\delta I$  from each measurement.

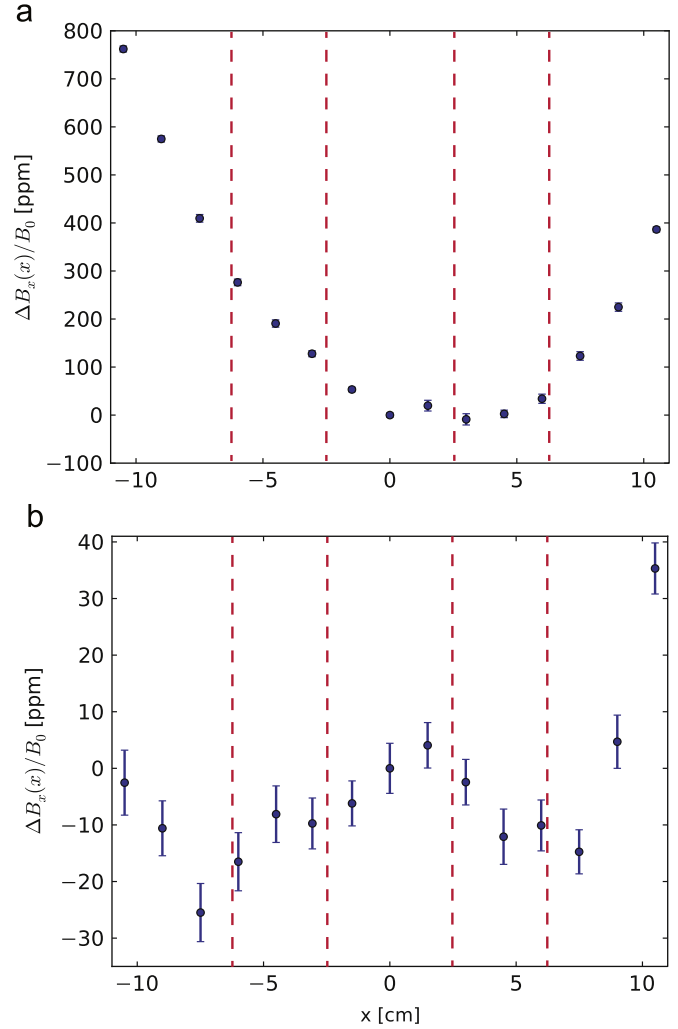


**Fig. 5.** Fractional  $B_x$  component of the field (a) before and (b) after optimization. The red-dashed lines mark the walls of the half-scale cells.  $\Delta B_x(x)$  corresponds to  $B_x(x) - B_x(0)$ . The measurements were taken on the line  $y=z=0$  with  $B_0 = 89.1$   $\mu$ T. (For interpretation of the references to color in this figure legend, the reader is referred to the web version of this article.)

The proportionality constant is given by the ratio of the average magnetic field and the average current.

We also correct the data for very slow changes in the magnetic environment. These include small fluctuations in the magnetic field of the laboratory or other more local changes like relaxation of the magnetic domains of the ferromagnetic material. We keep track of the slow changes by performing several interspersed measurements at  $x=y=z=0$ . This corresponds to the geometrical center of the  $B_0$  coil. We extract from these measurements a drift in the magnetic field  $dB_i/dt$  that can be used to correct the data taken in the interval  $dt$ . After the corrections, the error bar for a measurement of the magnetic field at a specific point in the lattice corresponds to residual RMS fluctuations which are of the order of 2.5 nT.

We extract the volume gradients of the magnetic field with the stabilized data off-line. The value of the gradient at a specific point is given by

$$\frac{\Delta B_j}{\Delta L_i} = \frac{B_j(q_i) - B_j(q_{i-1})}{q_i - q_{i-1}} \quad (5)$$

where  $B_j(q_i)$  is the component of the magnetic field in the  $j$ th direction evaluated in position  $q_i$  on the lattice.

**Table 3**  
Experimental fractional volume gradients of the magnetic field for  $B_0 = 89.1 \mu\text{T}$ .

	Left cell (ppm/cm)	Right cell (ppm/cm)
$\langle \partial B_x / \partial x / B_0 \rangle_{vol}$	3 (8.0)	−4.8 (11.5)
$\langle \partial B_y / \partial y / B_0 \rangle_{vol}$	−6.2 (4.4)	−10.7 (4.2)
$\langle \partial B_z / \partial z / B_0 \rangle_{vol}$	−1.32 (4.0)	9.5 (2.0)

**Table 4**  
Experimental fractional volume gradients of the magnetic field relevant for  $T_2$  for  $B_0 = 89.1 \mu\text{T}$ .

	Left cell (ppm/cm)	Right cell (ppm/cm)
$\langle  \partial B_x / \partial x / B_0  \rangle_{vol}$	89.6 (33.8)	109 (42.5)
$\langle  \partial B_x / \partial y / B_0  \rangle_{vol}$	51.4 (9.1)	59.5 (9.2)
$\langle  \partial B_x / \partial z / B_0  \rangle_{vol}$	9.6 (6.9)	16.1 (8.4)

Table 3 shows a typical set of gradients of the diagonal of the magnetic field gradient tensor relevant for the motional magnetic field systematic described in Section 2. We extract the error bars of our measurement from the random time fluctuations of the volume gradients over several hours. The error bars of the gradients related to  $B_x$  are larger than the other components due to the noise in the power supply that provides the current for the coil and the correlation between the more complex profile of  $B_x$  and the spacing of the positions at which we take our measurements. This behavior is directly related to the *in situ* gradient monitoring system and a more thorough explanation will be published elsewhere [32].

The  $B_0$  coil optimization design yielded a magnetic field with several spatial modes. Due to this, we expect slight asymmetries between gradients on both cells. For example, if  $B_x = kx^2$  where  $k$  is a constant, the gradients for  $x < 0$  and  $x > 0$  are different. In addition, asymmetries in the magnetic mass distribution around the volume of interest (misalignment between the nested magnetic shields and the existence of other magnetic material around the shields) might also induce asymmetries in the gradients. This same phenomenon might induce differences in the error bars between both cells besides the ones arising from periods with larger magnetic fluctuations during the full mapping cycle.

Experience has shown that in the room that contains the experimental setup (Synchrotron Laboratory at the California Institute of Technology), it is only possible to take measurements during quiet nights when anthropogenic magnetic noise is reduced. On average we obtain 5 complete good quality volume scans per night. A good data set has no large magnetic fluctuations and obeys the relation  $\nabla \cdot \vec{B} = 0$ .

Table 4 presents the gradients relevant for the calculation of  $T_2$ . Our coil minimizes the gradient responsible for the largest contribution to the transverse depolarization lifetime  $T_2$  ( $\partial B_x / \partial z$ ). Fig. 6 shows an example of the profile of this component.

The noisy magnetic environment in our laboratory and the limit of the sensitivity of the 3-axis magnetometer does not allow us to take data at low magnetic fields (a few  $\mu\text{T}$ ). We can, however, compare fractional gradients at different values of the magnetic field to determine how they scale. *A priori*, we expect the fractional gradients (and their time fluctuations) to be independent of the field (see Eq. (5)). If this requirement is fulfilled, the gradients at low fields can be obtained by multiplying the experimental fractional gradients by the desired magnetic field value.

Fig. 7 presents the projected fractional gradient  $\langle \partial B_x / \partial x / B_0 \rangle_{vol}$  for different values of the magnetic field for both left and right cells. We calculate these values by considering that the gradients

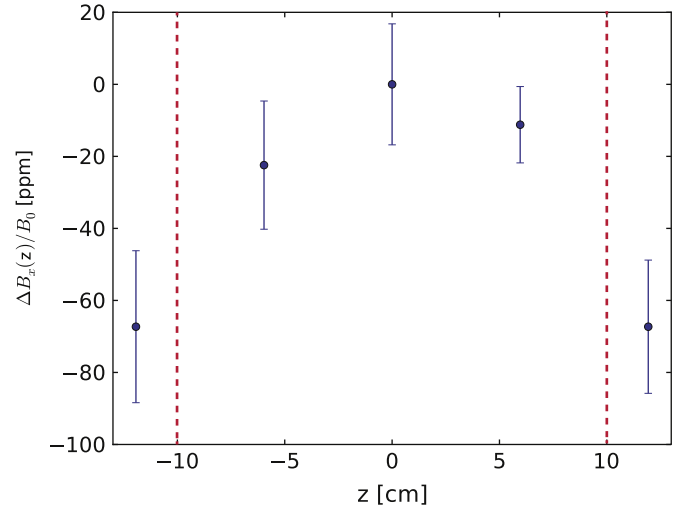


**Fig. 6.** Plot of  $\Delta B_x/B_0$  as a function of  $z$  for the half scale  $B_0$  coil. The red-dashed lines mark the walls of the half scale cell.  $\Delta B_x(z)$  corresponds to  $B_x(z) - B_x(0)$ . The measurements were taken on the line  $x = -5 \text{ cm}$ ,  $y = 0 \text{ cm}$  at  $B_0 = 89.1 \mu\text{T}$ . (For interpretation of the references to color in this figure legend, the reader is referred to the web version of this article.)

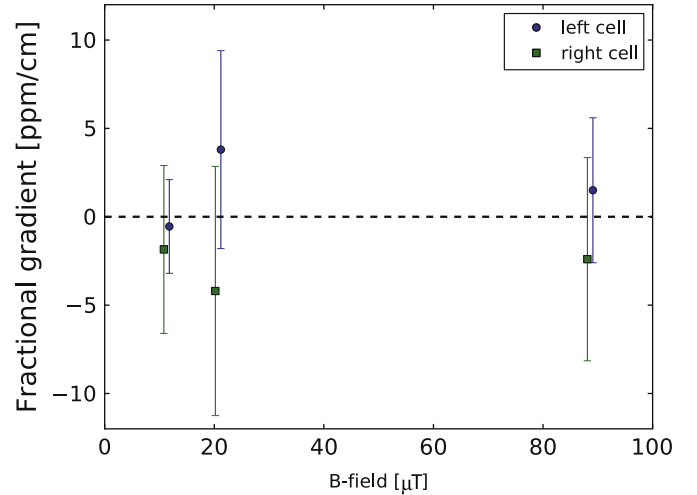


**Fig. 7.** Plot of the projected  $\langle \partial B_x / \partial x / B_0 \rangle_{vol}$  for the real size cells as a function of different values of the holding field for both half scale cells (see text for explanation).

are inversely proportional to the size of the magnetic coil and shields [33], *i.e.*, the gradients for the full scale system are a factor of two smaller than the experimental gradients. No strong dependence exists between the fractional gradients and the magnitude of the magnetic field thus bolstering the case for the functionality of the  $B_0$  coil at low fields.

## 5. Conclusions

We have presented work that will be used to design the main magnetic coil for the future search for a nEDM at Oak Ridge National Laboratory. The magnetic field gradients that define the performance of the coil have been evaluated in a half scale version. Table 5 summarizes the minimum requirements for the relevant gradients of the  $B_0$  coil as well as the projected gradients for the full scale system extrapolated from the experimental values considering an operating field of  $3 \mu\text{T}$ . The design of the prototype coil we present here is flexible enough that new sets of trimming coils can be incorporated, if needed, to optimize further

**Table 5**

Minimum requirements and projected values of the gradients. The projected gradients are calculated using a value of the magnetic field of 3  $\mu$ T.

Gradient	Requirement	Exp. value (left cell) (pT/cm)	Exp. value (right cell) (pT/cm)
$\langle \partial B_x / \partial x \rangle_{vol}$	10 pT/cm	4.5 (12)	−7.2 (17.1)
$\langle  \partial B_x / \partial z  \rangle_{vol}$	10 pT/cm	14.4 (10.5)	24.3 (12.6)

the magnetic environment, e.g., the addition of 5 wires per quadrant trimming coil.

## Acknowledgments

We thank R. Cortez for his skillful technical contributions to the design and fabrication of the automated measurement station and R. Golub for valuable discussions. This work was supported by the U.S. National Science Foundation, Grant No. PHY-0855538 and the U.S. Department of Energy, Grant No. DE-AC52-06NA25396.

## Appendix A

The wires on the surface of a  $\cos(\theta)$  coil follow the distribution [30]:

$$\cos(\phi_j) = 1 - \frac{2j-1}{2N}, \quad (\text{A.1})$$

where  $\phi_j$  is  $j$ th angle of the wire distribution,  $4N$  is the total number of wires on the coil, and  $j = 1, 2, \dots, N$ . If  $N = n_1 \cdot n_2$  where  $n_1$  is an odd number we can rewrite Eq. (A.1) as

$$\cos(\phi_j) = 1 - \frac{2j-1}{2n_1 \cdot n_2} = 1 - \frac{1}{2n_2} \left( \frac{2j-1}{n_1} \right), \quad (\text{A.2})$$

where the term inside the parenthesis will be an integer when  $2j-1$  is a multiple of  $n_1$ . For a given  $n_1$  and  $n_2$ , the subset of  $\phi_j$  that match this condition specifies another  $\cos(\theta)$  coil with  $N = n_2$ . We can superpose the coil with smaller number of turns on the larger one and use it to correct for small non-uniformities.

## References

- [1] S.K. Lamoreaux, R. Golub, J. Phys. G 36 (2009) 104002.
- [2] M.B. Gavela, et al., Phys. Lett. B 109 (1982) 215.
- [3] I.B. Khriplovich, A.R. Zhitnitsky, Phys. Lett. B 109 (1982) 490.
- [4] M. Pospelov, A. Ritz, Ann. Phys. 318 (2005) 119.
- [5] T.M. Ito, J. Phys.: Conf. Ser. 69 (2007) 012037.
- [6] R. Golub, S.K. Lamoreaux, Phys. Rep. 237 (1994) 1.
- [7] C.A. Baker, et al., Phys. Rev. Lett. 97 (2006) 131801.
- [8] R. Golub, D. Richardson, S.K. Lamoreaux, Ultracold Neutrons, Adam Hilger, Bristol, 1991.
- [9] J.M. Pendlebury, et al., Phys. Rev. A 70 (2004) 032102.
- [10] S.K. Lamoreaux, R. Golub, Phys. Rev. A 71 (2005) 032104.
- [11] A.L. Barabanov, R. Golub, S.K. Lamoreaux, Phys. Rev. A 74 (2006) 052115.
- [12] S.K. Lamoreaux, Phys. Rev. A 53 (1996) R3705.
- [13] L. Passell, R.I. Schermer, Phys. Rev. 150 (1966) 146.
- [14] Y. Abe, N. Morishima, Nucl. Instr. and Meth. A 459 (2001) 256.
- [15] N.F. Ramsey, Acta Physica Hungarica 55 (1984) 117.
- [16] G.L. Greene, et al., Phys. Rev. D 20 (1979) 2139.
- [17] J.L. Flowers, B.W. Petley, M.G. Richards, Metrologia 30 (1993) 75.
- [18] V.A. Dzuba, V.V. Flambaum, J.S.M. Ginges, Phys. Rev. A 76 (2007) 034501.
- [19] K. Green, et al., Nucl. Instr. and Meth. A 404 (1998) 381.
- [20] D.M. Ginsberg, M.J. Melchner, Rev. Sci. Instrum. 41 (1970) 122.
- [21] C.P. Slichter, Principles of Magnetic Resonance, Springer Verlag, Berlin, 1989.
- [22] D.D. McGregor, Phys. Rev. A 41 (1990) 2631.
- [23] R. Golub, R.M. Rohm, C.M. Swank, Phys. Rev. A 83 (2011) 023402.
- [24] R. Schmid, B. Plaster, B.W. Filippone, Phys. Rev. A 78 (2008) 023401.
- [25] S.K. Lamoreaux, et al., Europhys. Lett. 58 (2002) 718.
- [26] Document in preparation.
- [27] Metglas Inc. <www.metglas.com>.
- [28] Prime Conduit <www.primeconduit.com/VylonPipe.php>.
- [29] S. Malkowski, et al., Rev. Sci. Instrum. 82 (2011) 075104.
- [30] C. Bidinosti, I. Kravchuk, M. Hayden, J. Magn. Reson. 177 (2005) 31.
- [31] Bartington Instruments Ltd. <www.bartington.com>.
- [32] Document in preparation.
- [33] I.B. Khriplovich, S.K. Lamoreaux, CP Violation Without Strangeness, Springer Verlag, Berlin, 1997.